Physics informed DMD for periodic Dynamic Induction Control of Wind Farms

Muscari, C.; Schito, P.; Viré, A.; Zasso, A.; Van Der Hoek, D.; Van Wingerden, J. W.

DOI
10.1088/1742-6596/2265/2/022057

Publication date
2022

Document Version
Final published version

Published in
Journal of Physics: Conference Series

Physics informed DMD for periodic Dynamic Induction Control of Wind Farms

Physics informed DMD for periodic Dynamic Induction Control of Wind Farms

C Muscari[1,2], P Schito[1], A Viré[3], A Zasso[1], D van der Hoek[2] and JW van Wingerden[2]

[1] Politecnico di Milano, [2] TU Delft, Delft Center for Systems and Control (DCSC),
[3] TU Delft, Faculty of Aerospace Engineering, Wind Energy Section

E-mail: claudia.muscari@polimi.it

Abstract. Dynamic Induction Control (DIC) is a novel, exciting branch of Wind Farm Control. It makes use of time-varying control inputs to increase wake mixing, and consequently improve the velocity recovery rate of the flow and the power production of downstream turbines. The Pulse and the Helix are two promising DIC strategies that rely on sinusoidal excitations of the collective pitch and individual pitch of the blades, respectively. While their beneficial effects are evident in simulations and wind tunnel tests, we do not yet fully understand the physics behind them. We perform a systematic analysis of the dynamics of pulsed and helicoidal wakes by applying a data-driven approach to the analysis of data coming from Large Eddy Simulations (LES). Specifically, Dynamic Mode Decomposition (DMD) is used to extract coherent patterns from high-dimensional flow data. The periodicity of the excitation is exploited by adding a novel physics informed step to the algorithm. We then analyze the power spectral density of the resulting DMD modes as a function of the Strouhal number for different pitch excitation frequencies and amplitudes. Finally, we show the evolution in time and space of the dominant modes and comment on the recognizable patterns. By focusing on the modes that contribute the most to the flow dynamics, we gather insight on what causes the increased wake recovery rate in DIC techniques. This knowledge can then be used for the optimization of the signal parameters in complex layouts and conditions.

1. Introduction

Wind is leading the energy transition in Europe by meeting 16% of the power demand, but the EU Commission's ambition is to get it up to 50% by 2050 [1]. As the clustering of wind turbines closer and closer together in large farms is a standard by now, wind farm control emerges as a viable option for both enhancing power production and reducing maintenance costs [2].

In recent years, strategies involving time-varying control inputs have started gaining interest from the wind energy community. The main goal of these strategies is to promote the mixing of the wake with the surrounding airflow so that the inflow to the downstream turbines has a higher energy content. An early big step in this direction was done by Goit and Meyers [3], who described a procedure for finding the optimal dynamic induction of turbines in a wind farm. However, this was done at a high computational cost and resulted in a non-smooth signal. Munters and Meyers [4] observed that the optimal thrust coefficient signal in [3] resembled a sinusoid, which simplified the optimization problem significantly while reducing the detrimental effect on loads. The same results were reproduced experimentally by Frederik et al. [5]. The thrust coefficient was manipulated by exciting the collective pitch of the blades with a periodic

signal. This Dynamic Induction Control (DIC) technique was called the Pulse because of the magnitude variation's effect on the wake shape.

In 2020, Frederik et al. [6, 7] presented the Helix, a new concept that takes advantage of Individual Pitch Control (IPC), historically used for load mitigation, to dynamically vary the fixed-frame tilt and yaw moment to manipulate the wake. We refer to the Helix as a DIPC (Dynamic Individual Pitch Control) strategy. Preliminary tests lead to encouraging results: the Helix appears to increase power production without significantly increasing the loads on the blades when compared not only to the baseline greedy case but also to DIC as previously implemented in [4]. So far, not much effort has gone into understanding why these new strategies work so well. Filling this research gap requires a focus on wake dynamics.

Wakes can be described as high-dimensional, nonlinear dynamical systems characterized by multi-scale phenomena in both space and time. However complex, they often exhibit low-dimensional behavior. Wakes are the perfect example of a problem for which extensive data sequences can be readily available through computational fluid dynamics (CFD) while governing equations are complicated to grasp or formulate correctly. In these cases, a data-driven perspective can be adopted to complement more traditional model-based approaches. By applying modal decomposition techniques, we can represent the system with a number of modes that is orders of magnitude smaller than the state dimension of the system. The most common technique used for identifying coherent structures is Proper Orthogonal Decomposition (POD). POD determines spatial modes, which are ordered according to their energy content. It was first applied to fluid dynamics by Lumley [8]. In Rowley et al. [9], Dynamic Mode Decomposition (DMD) was introduced. It is also a data-driven approach; however, unlike POD, it produces modes based on their dynamics rather than the energy content and is characterized by a single frequency. The signal is split into a triplet of purely spatial modes, scalar amplitudes, and purely temporal signals. This makes it more suitable for the identification of dominant frequencies. Its applications to fluid dynamics in general and wind energy, in particular, include diagnostic and future state prediction. Various DMD algorithms have been developed and used for pattern detection, extraction of Reduced-Order Models (ROMs), and control. For example, Sun et al. [10] used DMD to investigate the near wake of a two-bladed horizontal axis wind turbine, gaining insight into the evolution of the tip vortices. In [11], Input-Output Dynamic Mode Decomposition (IODMD) was used to derive a ROM for yaw control, and this was extended in [12] with Koopman modes for wind farm control.

This work aims to provide insight into wakes manipulated with DIC and, in particular, into the phenomena that promote mixing. The analysis focuses on the most relevant coherent structures and their dependency on the DIC technique and excitation frequency. The exact DMD algorithm is employed for the coherent structures extraction and a novel physics informed (pi) step exploiting the periodicity of the DIC-related phenomena. The study is organized as follows: Section 2.1 is devoted to explaining DIC, describing the Pulse and the Helix. Section 2.2 presents the exact DMD algorithm with the extension of the pi step. Next, Section 3 introduces the setup of the LES. Section 4 provides a comparison between the baseline case (Greedy control), Pulse, and Helix (both clock-wise and counter-clockwise). We then study the dependency of wake dynamics on excitation frequency. Finally, we summarize our main conclusions and elaborate on possible further steps in Section 5.

2. Methods

2.1. Dynamic Induction Control

Control strategies based on a dynamically varying induction factor proved to increase the power production of small to medium-sized wind farms by enhancing wake mixing. With the unbounded optimal signal found in [3], DIC was able, in numerical simulations, to increase power gains up to 21% with respect to greedy control.

2.1.1. Pulse With the Pulse [5], wake mixing is induced by superimposing a sinusoidal signal on a wind turbine's collective blade pitch angles. The characterization of the excitation signal is usually done in terms of Strouhal number, which is its frequency f_e normalized with respect to the rotor diameter D and the free-stream velocity U_∞.

$$St = \frac{fD}{U_\infty} \tag{1}$$

In [4], Munters and Meyers found an optimal sinusoidal excitation for the thrust coefficient with an amplitude $A = 1.5$ and a Strouhal number $St = 0.25$. They also claim that, since these parameters are non-dimensional, this optimum should be robust to spacing and turbulence intensity.

2.1.2. Helix The Helix [6] uses IPC to achieve the same wake recovery effects as the Pulse, with lower fluctuations in power production and wake velocity. Instead of inducing an early wake breakdown by dynamically varying the thrust magnitude, IPC acts on its direction. This way, it imposes yaw and tilt moments on the rotor to force wake meandering [13]. These moments are excited with a low frequent sinusoidal signal with a certain phase offset, resulting in a moment rotating with a $1/f_e$ period. The multiblade coordinate (MBC) transformation projects the blade loads in a non-rotating reference frame. The resulting velocity field is helicoidal, hence the name of the strategy. If the phase offset between tilt and yaw angles is equal to $\pi/2$, the Helix rotates in counter clock-wise (CCW) direction; if it is equal to $\frac{3}{2}\pi$, the Helix rotates in clock-wise (CW) direction. The preliminary tests in [6] show that the CCW-Helix leads to faster wake recovery than CW-Helix.

2.2. Physics Informed Dynamic Mode Decomposition
With DMD, we can extract key spatial invariant modes and their corresponding temporal response. This section briefly summarizes the main steps taken in the regular DMD algorithm and how knowledge related to the excitation can be incorporated into the algorithm.

The first step is to collect m snapshots of the flow field. These snapshots are representative of the state of the system at each time step, reshaped into a very tall column vector. In this paper we define this state vector as:

$$x_k = \begin{bmatrix} u(t_k)^T & v(t_k)^T & w(t_k)^T & p(t_k)^T \end{bmatrix}^T \in \mathbb{R}^{n\times 1}, \tag{2}$$

where $u(t_k)$, $v(t_k)$, $w(t_k)$ represent the vectorized velocity fields in the 3 dimensions at time instance t_k, and $p(t_k)$ contains the pressure field in the whole computational domain. We can organize the snapshots into the matrices X and X':

$$X = \begin{bmatrix} \vdots & \vdots & \vdots & & \vdots \\ x_1 & x_2 & x_3 & \dots & x_{m-1} \\ \vdots & \vdots & \vdots & & \vdots \end{bmatrix} \in \mathbb{R}^{n\times m-1}, \quad X' = \begin{bmatrix} \vdots & \vdots & \vdots & & \vdots \\ x_2 & x_3 & x_4 & \dots & x_m \\ \vdots & \vdots & \vdots & & \vdots \end{bmatrix} \in \mathbb{R}^{n\times m-1}, \tag{3}$$

with $n \in \mathbb{Z}^+$ the state dimension and $m \in \mathbb{Z}^+$ the number of snapshots. Linear DMD then finds the best linear operator that advances X into X':

$$X' \approx AX \qquad\qquad (x_{k+1} = Ax_k)\,. \tag{4}$$

When the state dimension n is very large, it is unfeasible to deal with the full $A \in \mathbb{R}^{n\times n}$ matrix directly. The DMD algorithm substitutes it with a POD-projected matrix $\widetilde{A} \in \mathbb{R}^{r\times r}$ with r

the reduced state dimension. This matrix is obtained using the Singular Value Decomposition (SVD) of X

$$X \approx U\Sigma V^*, \tag{5}$$

where $*$ denotes the complex conjugate transpose, $U \in \mathbb{C}^{n\times r}$, $\Sigma \in \mathbb{C}^{r\times r}$ and $V \in \mathbb{C}^{m\times r}$. The left singular vectors $\mathbf{U}$ are POD modes. The columns of $\mathbf{U}$ are orthogonal, so $U^*U = I$; similarly $V^*V = I$. The matrix $\widetilde{A}$ can thus be written as

$$\widetilde{A} = U^*AU = U^*X'V\Sigma^{-1}. \tag{6}$$

The following step is the eigen-decomposition of $\widetilde{A}$:

$$\widetilde{A}W = W\Lambda, \tag{7}$$

where the columns of $W \in \mathbb{C}^{r\times r}$ are eigen-vectors and $\Lambda \in \mathbb{C}^{r\times r}$ is a diagonal matrix containing the corresponding eigenvalues $\lambda_k \in \mathbb{C}$. At this point we exploit the fact that we work with a periodic excitation signal to develop a physics informed DMD scheme. For presentation reasons, we will first convert the autonomous dynamic equation (4) into its continuous time equivalent:

$$\frac{dx}{dt} = \tilde{A}_c x \tag{8}$$

Next, we exploit the fact that the response contains a first-order rigid body mode (mean of the flow field) and a number of undamped second-order oscillatory modes (excitation frequency and higher harmonics). With this information, there exists a similarity matrix $T \in \mathbb{C}^{r\times r}$ such that TAT^{-1} is a structured real block diagonal matrix. The new linear operator $\hat{A}_c = T\tilde{A}_cT^{-1}$ has the same eigenvalues as $\tilde{A}_c$ and has the following block diagonal structure:

$$\hat{A}_c = \begin{bmatrix} 0 & & & & & & & \\ & 0 & \omega_1 & & & & & \\ & -\omega_1 & 0 & & & & & \\ & & & 0 & \omega_2 & & & \\ & & & -\omega_2 & 0 & & & \\ & & & & & \ddots & & \\ & & & & & & 0 & \omega_q \\ & & & & & & -\omega_q & 0 \end{bmatrix}, \tag{9}$$

where q represents the number of harmonic modes we take into account. The time-invariant modal shapes are subsequently given by:

$$\begin{bmatrix} \Phi^{(0)} & \Phi_1^{(1)} & \Phi_2^{(1)} & \dots & \Phi_1^{(q)} & \Phi_2^{(q)} \end{bmatrix} = X'V\Sigma^{-1}WT^{-1} \in \mathbb{R}^{n\times 2q+1}, \tag{10}$$

[1]

with $\Phi_*^{(*)} \in \mathbb{R}^{n\times 1}$. This makes it possible to describe the flow from a given set of initial conditions $\alpha(t_1)$ at time instance t_1 into a response at time instance t_2 as a summation of modes:

$$\begin{bmatrix} u(t_2) \\ v(t_2) \\ w(t_2) \\ p(t_2) \end{bmatrix} = \Phi^{(0)}\alpha^{(0)}(t_1) + \sum_{i=1}^{q} \begin{bmatrix} \Phi_1^{(i)} & \Phi_2^{(i)} \end{bmatrix} \begin{bmatrix} \cos(\omega_i\Delta t) & \sin(\omega_i\Delta t) \\ -\sin(\omega_i\Delta t) & \cos(\omega_i\Delta t) \end{bmatrix} \begin{bmatrix} \alpha_1^{(i)}(t_1) \\ \alpha_2^{(i)}(t_1) \end{bmatrix}, \tag{11}$$

with $\Delta t = t_2 - t_1$ and $\alpha_*^{(*)}(t_1)$ the initial condition of a corresponding mode at time instance t_1. With the normalization of the mode shapes we can now track the modal amplitudes over time: for mode 0 (the mean mode) it will be $||\Phi^{(0)}\alpha^{(0)}||_F$, for the second order ones it can be computed as $\sqrt{\left(\left|\left|\Phi_1^{(i)}\alpha_1^{(i)}(t_1)\right|\right|_F^2 + \left|\left|\Phi_2^{(i)}\alpha_2^{(i)}(t_1)\right|\right|_F^2\right)}$, with $||*||_F$ the Frobenius norm.

[1] A full derivation of this equation can be found in [14]

3. Simulation

The snapshots given as input for the DMD were obtained from a Large Eddy Simulation (LES) performed in SOWFA [15] coupled to the super controller described in [16]. The rotor is modeled with the Actuator Line Model (ALM), an extension of the Blade Element Momentum (BEM) method for hybrid CFD/analytical computations. The Atmospheric Boundary Layer (ABL) flow is governed by an incompressible formulation of the Navier-Stokes (NS) equations, while the model substitutes the physical blades with body forces distributed along lines that represent them. The forces are obtained through tabulated airfoil data and projected back into the domain employing a three-dimensional smearing Gaussian function to prevent numerical issues. Its main advantage is that it drastically reduces the computational cost while maintaining high fidelity results.

For our study, we used a uniform inflow profile to isolate the effect of the pitch actuation. The wind speed at hub height was set to $9\,m/s$. These conditions are not representative of realistic working conditions in an actual wind farm, but they are perfectly suited to visualize the effects of DIC on the wake. The considered rotor is the DTU 10 MW reference turbine [17], which has a diameter of $178.3\,m$. The simulated time is $2000\,s$ but, for our snapshots, we discard the transient part, corresponding to the initial $400s$. The simulation time step is $0.2s$. The base mesh has the characteristics described in Table 1 and was locally refined to reach a characteristic cell dimension in the rotor area of $3.125\,m$. For the snapshots, we further decimated the data in space by considering one out of four elements in x, y, and z.

Table 1. Base mesh characteristics. Direction x is stream-wise, y is vertical, z is perpendicular to x and y.

	x	y	z
domain extension	2500 m	1000 m	600 m
number of cells	50	20	12

3.1. ALM optimal parameters

The requirements on the parameters imposed by the use of the ALM were respected: the projection function width was set to circa twice the characteristic cell dimension, i.e. $6m$. The choice of the correct value for this parameter is of the utmost importance. The reason is quite intuitive: if a very large value is chosen, the actuator line model will appear to recover an aerodynamic power exceeding the Betz limit, and if too small a value is chosen, the predicted power will be well below measurements or BEM calculations. The number of cells along a blade was higher than 50, which guaranteed an accurate description of the tip vortices.

4. Analysis

The data structure obtained from the simulation has dimensions of $96000 \times 800 \times 4$. The first dimension is space, the second time, then, for each spatio-temporal coordinate, we have collected all three velocity components and pressure. We reorganized it in column vectors that we feed to the DMD algorithm described in Section 2.2. The selected rank for our decomposition is 9, which means that we will obtain nine complex-conjugate eigenvalues and four modes in addition to mode 0. The choice of the rank is justified by the results in Table 2.

The sampling interval and the number of snapshots did not undergo a sensitivity analysis because, in other studies, the variation of the residual resulted to be insensitive to the former [18, 19], and to reach a plateau for the latter exactly around $m = 800$ [18] .

Table 2. Goodness of fit (FIT_{total}) of the decomposition measured through Variance Accounted For (VAF) between original and reconstructed data structure for the cases with St equal to 0.25. FIT_{out} is computed leaving that particular mode out of the reconstruction.

	FIT_{total}	FIT_{out} 0	FIT_{out} 1	FIT_{out} 2	FIT_{out} 3	FIT_{out} 4
Pulse	98.08	21.55	81.52	94.26	97.79	98.08
CW Helix	98.38	25.17	77.52	95.05	97.37	98.36
CCW Helix	97.77	28.08	75.44	93.95	95.84	97.75

4.1. Pulse and Helix comparison to baseline case

In the first part of the analysis, we compare the wakes resulting from Pulse, CW-Helix, and CCW-Helix. We consider data coming from three simulations with the setup described in Section 3. In all three cases, we consider a signal with 4° amplitude and St equal to 0.25. In Table 3, we summarize the characteristics of the found DMD modes. The first thing we notice is that, for the DIC cases, the frequencies associated with these modes are recognizable and definitely not surprising: modes 1, 2, and 3 are respectively excited by the DIC signal frequency and its first and second harmonics. The frequency associated with mode 4 is the rotor frequency 1P. The modal amplitudes show that Mode 0 is always dominant. It is interesting to observe how Mode 4 seems to be insignificant for the Pulse data while for both the Helix cases, its modal amplitude is higher than the one associated with Mode 3.

Table 3. Frequencies and individual contribution to the reconstruction given by each one of the five most relevant DMD modes.

	Pulse		CW-Helix		CCW-Helix	
	St	Modal Amplitude	St	Modal Amplitude	St	Modal Amplitude
mode 0	0	1	0	1	0	1
mode 1	0.25	0.240	0.25	0.160	0.25	0.151
mode 2	0.5	0.130	0.5	0.092	0.5	0.083
mode 3	0.75	0.069	0.75	0.057	0.75	0.059
mode 4	2.7	0.0003	2.7	0.064	2.7	0.064

Mode 0, being associated with zero frequency, is representative of the mean flow. We chose to represent this mode separately because it gives a more immediate visualization of the DIC techniques' effect on the recovery rate. We also plot it for the baseline case (same setup but static greedy control) in Fig. 1. The effectiveness of the three DIC techniques is immediately apparent: the wind speed in the wake for the baseline case is uniformly low (about half the free-stream velocity), and the wake itself is significantly longer than in the remaining cases. In the near wake, which is 1 to 4 diameters downstream of the turbine, we do not notice huge differences between Pulse and CW-helix. The high-velocity zone in the hub region derives from the fact that we do not model the nacelle. Interestingly, for the CCW-helix, starting from 3D diameters downstream, an area of significantly (20%) lower wind speed appears. This area prolongs in the middle part between 4 and 6 diameters, where we start to spot bigger differences also between Pulse and CW-helix. For CW-helix, the higher variability in wind speeds is representative of an enhanced mixing. At the same time, we notice that full recovery of the outer part starts earlier in the pulsed wake. The far wake is the most interesting for our purposes and in terms

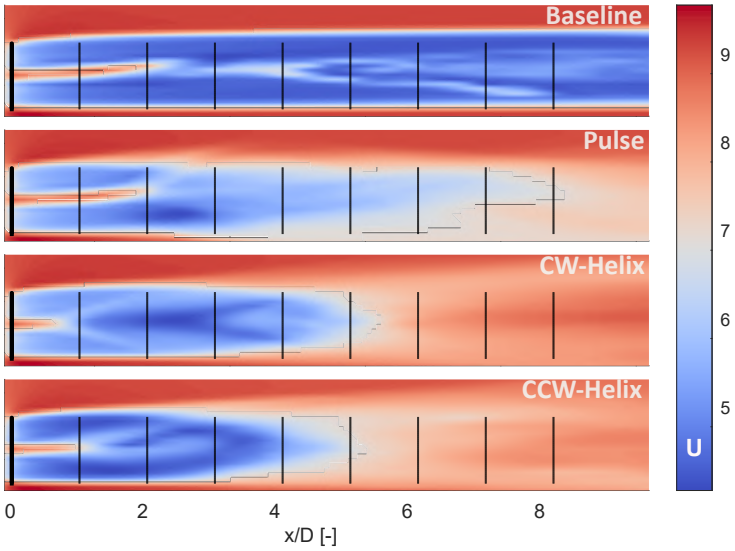

Figure 1. Vertical slices of the stream-wise velocity component, reconstructed from mode 0 as $\Phi^{(0)}\alpha^{(0)}$. From top to bottom, we have Pulse, CW-Helix, and CCW-Helix. The free-stream velocity was 9 m/s.

of differences between the DIC techniques considered. The CCW-helix is the only technique leading to recovering up to 80% of the free-stream velocity before the flow reaches a distance correspondent to five diameters downstream. Concerning the Pulse, the big difference in velocity between the center of the wake and its borders suggests higher turbulence levels that would negatively affect a second turbine placed at that distance. Furthermore, the pulsed far wake is asymmetric, which could impact the loads distribution in a wind farm setting. This analysis confirms and extends what was observed in [6].

Additional information can be given by the remaining four modes, which represent oscillations around the mean flow. We show them through iso-surfaces of velocity in Fig. 2. Since we had uniform flow and no pitch actuation, the remaining modes for the baseline case are associated with higher frequencies and have no significance for our analysis. Iso-values for Fig. 2 are chosen so that they give a good visual representation of the mode, and they are different for the different modes. The obtained tridimensional visualization of the modes gives us valuable information. First of all, we can really see how the mode shapes respectively pulsate and rotate helicoidally in alternate directions. We can also evidence how, together with harmonic growing of the frequency, the structures become closer together. An interesting feature of the Helix shapes is that they seem to enlarge as they move downstream before breaking down, while for the Pulse, the main structure repeats itself a few times before disassembling.

4.2. Pulse and CCW-Helix modes dependence on Strouhal number

With the same setup described in Section 3 ($St = 0.25$), the Pulse and CCW-Helix simulations were repeated for Strouhal numbers equal to 0.2, 0.3, and 0.4. The amplitude remained unvaried and equal to 4°. This was done to assess the influence of this parameter on the mixing dynamics. The DMD analysis was performed as described in Section 4, and Table 4 summarizes the main findings. Again, as expected, the frequencies associated with the modes follow a very clear pattern: a mode with 0 frequency associated with the mean flow, a mode with the same frequency as the one associated with the DIC signal frequency, two with higher harmonics of this same frequency and finally one related to the rotation frequency of the rotor.

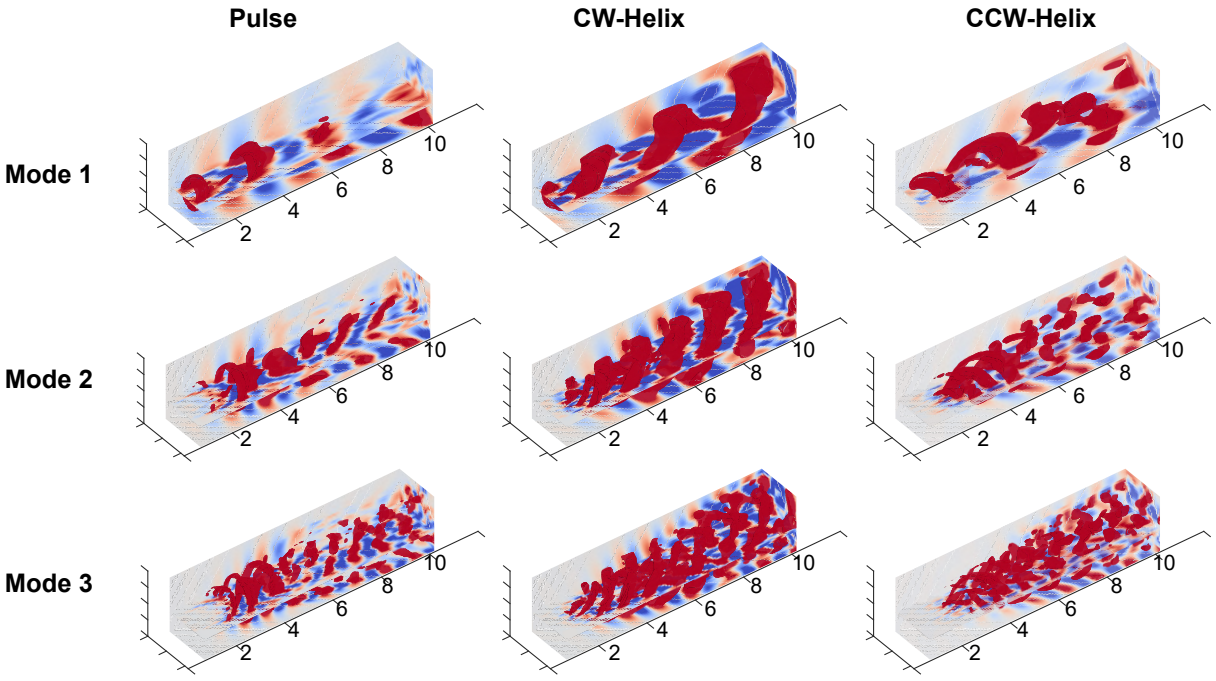

Figure 2. Iso-surfaces of the stream-wise velocity component reconstructed from modes 1, 2, and 3 (from top to bottom) as $\Phi_1^{(i)}\alpha_1^{(i)}(t_1)$ with i equal to 1,2,3 respectively. From left to right, we have Pulse, CW-Helix, and CCW-Helix. The free-stream velocity was 9 m/s. Three slices, positioned at the left, bottom, and downstream boundaries of the domain, are added to improve visualization

Table 4. Frequencies and energy associated with the four most relevant DMD modes (after mode 0) for Pulse and CCW-Helix simulations at different excitation St numbers.

	Mode 1			Mode 2			Mode 3			Mode 4		
	St	Modal Amplitude		St	Modal Amplitude		St	Modal Amplitude		St	Modal Amplitude	
		Pulse	CCW-Helix		Pulse	CCW-Helix		Pulse	CCW-Helix		Pulse	CCW-Helix
St 0.20	0.20	0.226	0.143	0.4	0.139	0.078	0.6	0.075	0.055	2.7	0.004	0.063
St 0.25	0.25	0.240	0.151	0.5	0.130	0.083	0.75	0.069	0.059	2.7	0.0003	0.065
St 0.30	0.30	0.243	0.158	0.6	0.119	0.082	0.9	0.059	0.055	2.7	0.001	0.065
St 0.40	0.40	0.234	0.192	0.8	0.101	0.100	1.2	0.029	0.050	2.7	0.0009	0.065

By plotting vertical slices of the stream-wise velocity component for mode 0, we can visualize the mean flow evolution in stream-wise direction in Fig. 3. Also for the other tested frequencies, the CCW-Helix appears to be more effective in enhancing the mixing: immediately downstream of the rotor we have a stronger deficit but the wake is shorter. The Pulse slices confirm the results of [4]: the fastest recovery is observed for $St = 0.25$. The difference with $St = 0.2$ is minimal. Interestingly, the latter has a more symmetrical wake, which could be relevant when optimizing the signal taking downstream turbines loading into account. Much more interesting is the representation of mode 0 for the CCW-Helix, which suggests that the optimal excitation frequency for this technique is higher than for the Pulse. The remaining modes are represented in Fig. 4. The frequencies follow the same pattern evidenced in Section 4.1. When the wake

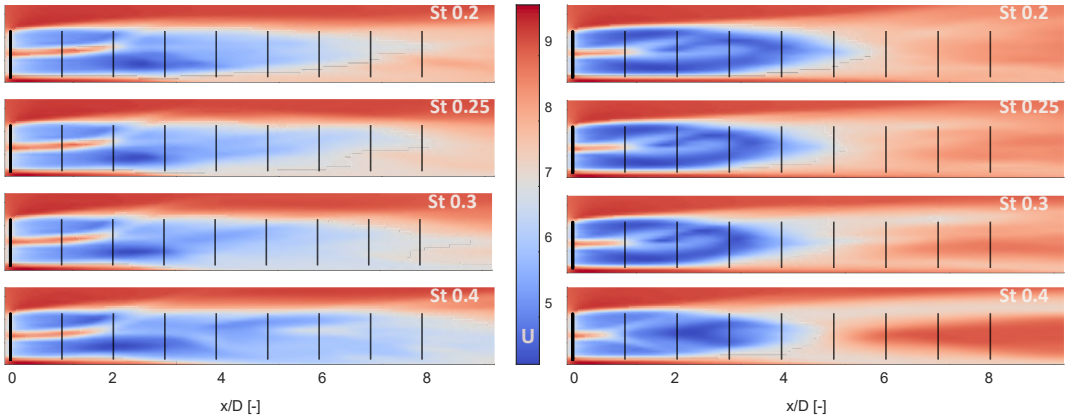

Figure 3. Vertical slices of the stream-wise velocity component reconstructed from mode 0 as $\Phi^{(0)}\alpha^{(0)}$. Slices on the left are relative to Pulse simulations. Slices on the right to CCW-Helix simulations. Each slice from top to bottom corresponds to a different St number for the excitation signal.

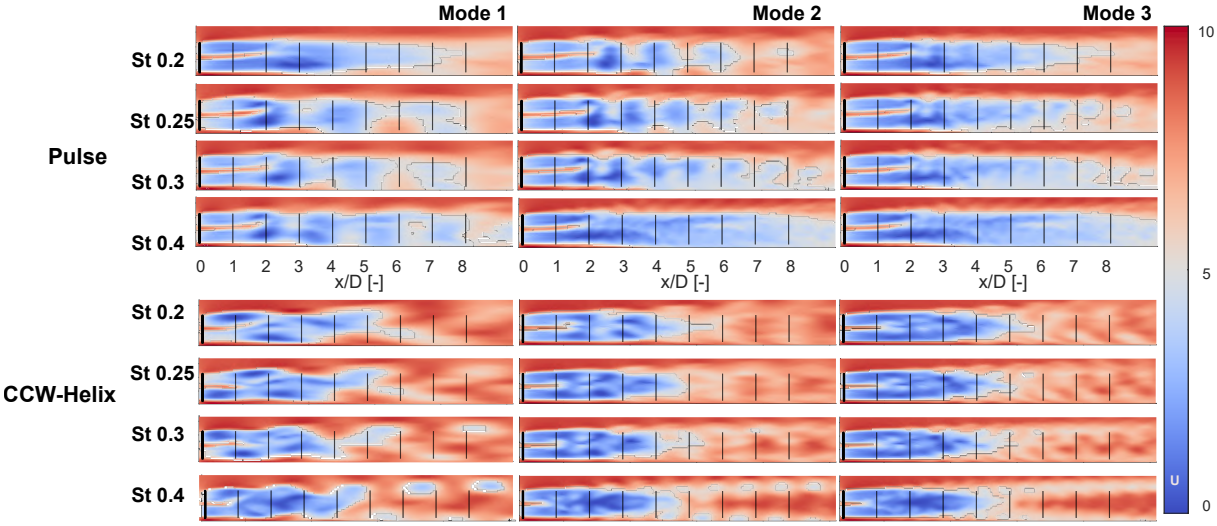

Figure 4. Vertical slices of stream-wise velocity at y=0,reconstructed from modes 1, 2, and 3 (from left to right) as $\Phi_1^{(i)}\alpha_1^{(i)}(t_1)$ with i equal to 1,2,3 respectively, for Pulse and CCW-Helix simulations for all of the considered St numbers.

breakes we can even see how the number of distinct structures doubles from one mode to the next.

5. Conclusions

In this paper, we reported the results of a numerical study aimed at characterizing the dynamic response of wakes manipulated with DIC techniques. The considered turbine was the DTU 10 MW. Its operation under a uniform inflow was simulated using the CFD framework SOWFA with the blades modeled as actuator lines. The obtained data structure was analyzed via a novel piDMD algorithm retrieving the five most relevant dynamic modes associated with the wake. Appropriate representations of these modal shapes were used to compare two promising DIC techniques, namely the Pulse and the Helix, and assess the dependence of their effectiveness in

increasing the mixing on the pitch excitation frequency. As a consequence of the periodicity of the excitation signal, the frequencies associated with the three most relevant modes are the excitation frequency and its first and second harmonics. The modes associated to the Helix have helicoidal shapes that enlarge as they travel downstream and have pitches proportional to the mode frequency. The CCW-Helix is the technique leading to the quickest recovery to the free-stream velocity. This is consistent with the findings of Frederik et al. [6]. The fastest recovery for the Pulse is observed for St equal to 0.25, while the Helix is more effective for the highest St tested ($St = 0.4$). The higher modes give us an idea of the regions where dynamically interesting phenomena can be observed and of the frequencies associated with them. They could guide a selection of appropriate subdomains we could limit further analysis to. Future works will extend the analysis for the Helix to higher St numbers and assess the dependence on the excitation amplitude, also for simple wind farm cases.

References

[1] EU Commission. A european green deal, 2019.
[2] van Wingerden JW, Fleming PA, Göçmen T, Eguinoa I, Doekemeijer BM, Dykes K, Lawson M, Simley E, King J, Astrain D et al. Expert elicitation on wind farm control. In *J. of Phys.: Conf. Series*, volume 1618, page 022025. IOP Publishing, 2020.
[3] Goit JP and Meyers J. Optimal control of energy extraction in wind-farm boundary layers. *J. Fluid Mech.*, 768:5–50, 2015.
[4] Munters W and Meyers J. Towards practical dynamic induction control of wind farms: analysis of optimally controlled wind-farm boundary layers and sinusoidal induction control of first-row turbines. *Wind Energy Science*, 3(1):409–425, 2018.
[5] JA Frederik, R. Weber, S. Cacciola, F. Campagnolo, A. Croce, C. Bottasso, and J.W. van Wingerden. Periodic dynamic induction control of wind farms: proving the potential in simulations and wind tunnel experiments. *Wind Energy Science*, 5(1):245–257, 2020.
[6] Frederik JA, Doekemeijer BM, Mulders SP and van Wingerden JW. The helix approach: Using dynamic individual pitch control to enhance wake mixing in wind farms. *Wind Energy*, 23(8):1739–1751, 2020.
[7] Frederik J,, Doekemeijer B, Mulders S, and van Wingerden JW. On wind farm wake mixing strategies using dynamic individual pitch control. In *J. Phys.: Conf. Series*, volume 1618, page 022050. IOP Publishing, 2020.
[8] Lumley JL. The structure of inhomogeneous turbulent flows. *Atmospheric turbulence and radio wave propagation*, 1967.
[9] Rowley CW, Mezić I, Bagheri S, Schlatter P and Henningson DS. Spectral analysis of nonlinear flows. *J. fluid Mech.*, 641:115–127, 2009.
[10] Sun C, Tian T, Zhu X, Hua O and Du Z. Investigation of the near wake of a horizontal-axis wind turbine model by dynamic mode decomposition. *Energy*, 227:120418, 2021.
[11] Cassamo N and van Wingerden JW. Model predictive control for wake redirection in wind farms: a koopman dynamic mode decomposition approach. In *2021 American Control Conf. (ACC)*, pages 1776–1782. IEEE, 2021.
[12] Cassamo N and van Wingerden JW. On the potential of reduced order models for wind farm control: A koopman dynamic mode decomposition approach. *Energies*, 13(24), 2020.
[13] Kimura K, Tanabe Y, Matsuo Y, and Iida M. Forced wake meandering for rapid recovery of velocity deficits in a wind turbine wake. In *AIAA Scitech 2019 Forum*, page 2083, 2019.
[14] Jonathan H Tu. *Dynamic mode decomposition: Theory and applications*. PhD thesis, Princeton University, 2013.
[15] Churchfield M, Lee S and Moriarty P. Overview of the simulator for wind farm application (SOWFA). *NREL*, 2012.
[16] Fleming P, Gebraad P, van Wingerden JW, Lee S, Churchfield M, Scholbrock A, Michalakes J, Johnson K. and Moriarty P. SOWFA super-controller: A high-fidelity tool for evaluating wind plant control approaches. Technical report, National Renewable Energy Lab.(NREL), Golden, CO (United States), 2013.
[17] Bak C, Zahle F, Bitsche R, Kim T, Yde A, Henriksen LC, Hansen MH, Blasques JPAA, Gaunaa M and Natarajan A. The DTU 10-MW reference wind turbine. In *Danish Wind Power Research 2013*, 2013.
[18] Sarmast S, Dadfar R, Mikkelsen RF, Schlatter P, Ivanell S, Sørensen JN and Henningson DS. Mutual inductance instability of the tip vortices behind a wind turbine. *J. Fluid Mech.*, 755:705–731, 2014.

[19] Schmid PJ. Dynamic mode decomposition of numerical and experimental data. *J. fluid Mech.*, 656:5–28, 2010.